Electrically Small, Planar, Frequency-Agile, Beam-Switchable Huygens Dipole Antenna

Zhentian Wu, *Student Member, IEEE*, Ming-Chun Tang, *Senior Member, IEEE*, and Richard W. Ziolkowski, *Life Fellow, IEEE*

***Abstract* — An electrically small, planar, frequency-agile, beam-switchable Huygens dipole antenna is investigated in this paper. The near-field resonant parasitic (NFRP) design incorporates an Egyptian axe dipole (EAD) and a capacitively loaded loop (CLL) that function as the electric and magnetic NFRP elements, respectively. A varactor diode is integrated into each of these NFRP elements to facilitate simultaneous tuning of its operating frequency and switching its main beam direction. By changing the capacitance values of these two varactor diodes, the antenna realizes two independent, antipodal, unidirectional endfire radiating states with similar realized gain (RG) and front-to-back ratio (FTBR) values within virtually the same frequency-agile ranges. The experimental results demonstrate that the developed antenna exhibits a 5.0% frequency-agile fractional impedance bandwidth in both of its two oppositely directed endfire states. The antenna is electrically small at the highest frequency of this bandwidth (ka_{high} < 0.86) and has measured relatively high radiation efficiency (RE > 67.7%), peak RG (2.1–3.19 dBi) and FTBR (5.61–13.4 dB) values, together with stable and uniform radiation patterns, over this frequency-agile range.**

***Index Terms* — Beam-switchable antennas, electrically small antennas, frequency-agile antennas, Huygens dipole antennas, planar antennas.**

I. Introduction

Electrically small antennas (ESAs) with exceptional performance characteristics have been investigated extensively in recent years. They are advantageous for many fifth generation (5G) and beyond internet-of-things (IoT) applications [1]. In particular, the pursuit of high-directivity ESAs has led to a variety of designs. A very productive approach has been developed by organically combining electrically small electric and magnetic near-field resonant parasitic (NFRP) elements to achieve electrically small Huygens dipole antennas (HDAs). They have achieved high directivities, large front-to-back ratios (FTBR) and wide beamwidths without the requirement of additional constructs such as reflector elements [2], periodic electromagnetic band gap structures [3], or slot structures [4]. A variety of electrically small HDAs have been reported. These include passive versions, such as single linearly [5]-[9] (LP) and circularly polarized [10], [11] (CP) designs, dual-LP systems [12], as well as active versions, which include reconfigurable [13-14] and non-Foster designs [15]. Nonetheless, in order to meet the versatility required for modern wireless communication platforms, multifunctional electrically small HDAs would be welcomed.

A number of ESAs with reconfigurable performance characteristics have been reported recently in the literature [13-14, 16-17]. On the one hand, systems with frequency-agile or frequency-reconfigurable performance have been developed, e.g., PIFA [16] and loop [17] designs using varactor diodes, and frequency reconfigurable complementary structure designs using p-i-n diodes [13]. On the other hand, RF switch-based systems focused on pattern-reconfigurable performance, e.g., end-fire radiating Huygens dipole designs, have also appeared [14]. A reconfigurable driven element with two p-i-n diodes is introduced in [14] that selectively excites the requisite NFRP elements to achieve two unidirectional endfire states in the fixed frequency band, each state radiating in opposite directions. However, one finds that it is a challenge to achieve reconfigurable patterns with a frequency-reconfigurable ESA and, likewise, to realize frequency reconfigurability with a pattern-reconfigurable ESA. To the best of our knowledge there is no single ESA system currently available that can perform both frequency and pattern reconfigurable functions. Therefore, it is highly desirable to develop one. It would be quite suitable for many modern space-limited wireless platforms that must perform multiple functions for advanced land, water and space based applications [18], [19]. An electrically small, planar, frequency-agile, beam-switchable NFRP HDA is developed in this paper. Its NFRP elements include versions of the electric Egyptian axe dipole (EAD) and of the magnetic capacitively loaded loop (CLL) tailored to enable these multiple functions. A varactor diode is integrated into each of these NFRP elements to achieve both the frequency and pattern reconfigurabilities without requiring any additional matching

Manuscript received on November 19, 2020; revised on April 11, 2021; and accepted on May, 25, 2021…

This work was supported in part by the National Natural Science Foundation of China contract number 62061006, in part by the Graduate Scientific Research and Innovation Foundation of Chongqing, China contract number CYB20066, in part by the Chongqing Natural Science Foundation contract number cstc2019jcyjjqX0004, and in part by the Australian Research Council grant number DP160102219. *(Corresponding author: Ming-Chun Tang.)*

Z. Wu and M.-C. Tang are with the Key Laboratory of Dependable Service Computing in Cyber Physical Society Ministry of Education, College of Microelectronics and Communication Engineering, Chongqing University, Chongqing 400044, China (E-mail: tangmingchun@cqu.edu.cn).

R. W. Ziolkowski is with the University of Technology Sydney, Global Big Data Technologies Centre, Ultimo NSW 2007, Australia (E-mail: Richard.Ziolkowski@uts.edu.au).

networks. Two unidirectional endfire states are obtained with virtually the same frequency-agile ranges. Note that the pattern reconfigurable performance characteristics in [14] are realized by integrating the PIN diodes on the driven element. In contrast, the varactor diodes are separately integrated into the NFRP elements in this design, which would accomplish more degrees of freedom to simultaneously obtain the frequency and pattern reconfigurabilities. The antenna configuration and its design principles are detailed in Section II. The prototype of this design that was fabricated and measured is described in Section III. The measured results will be shown to be in good agreement with their simulated values. Moreover, the physical mechanisms that lead to both its frequency and pattern reconfigurable functions will be discussed in detail to provide a more comprehensive understanding of the design principles. Finally, conclusions are drawn in Section IV.

We note that this innovative frequency and pattern reconfigurable ESA is a significant advancement from the previous, closely related design reported in [14]. In comparison, the frequency-agile, beam-switchable HDA developed herein consists of only a single HDA and a simple dipole as the driven element instead of two separate HDAs with a complex driven element. Consequently, it reduces the complexity of the antenna system by half. Moreover, the reported antenna utilizes the same number of diodes (two varactor diodes) to achieve both frequency-agility and beam-reconfigurability instead of simply a switchable beam at a fixed frequency (two p-i-n diodes). Furthermore, the combination of frequency and pattern reconfigurability in a simple, electrically small HDA provides a multifunctional solution that is readily integrated into size-constrained platforms where diversity schemes are employed to improve the system performance, e.g., for environmentally agnostic communication [16] and anti-jamming communication [17] systems.

All of the numerical simulations and their optimizations reported herein were performed using the frequency domain, finite-element-based ANSYS/ANSOFT high-frequency structure simulator, version 18.0. The simulation models employed the known, real properties of the dielectrics and conductors.

II. Frequency-Agile, Beam-Switchable HDA Design

Fig. 1 illustrates the design details of the developed planar, frequency-agile, beam-switchable Huygens dipole ESA. The entire system consists of only one Rogers Duroid™ 5880 copper-clad teflon substrate with its thickness $h1$ = 0.508 mm and radius $R1$ = 26.5 mm. It has a relative dielectric constant ε_r = 2.2, loss tangent tan δ = 0.0009, and 0.017 mm copper cladding thickness. The optimized design parameters are given in Table I.

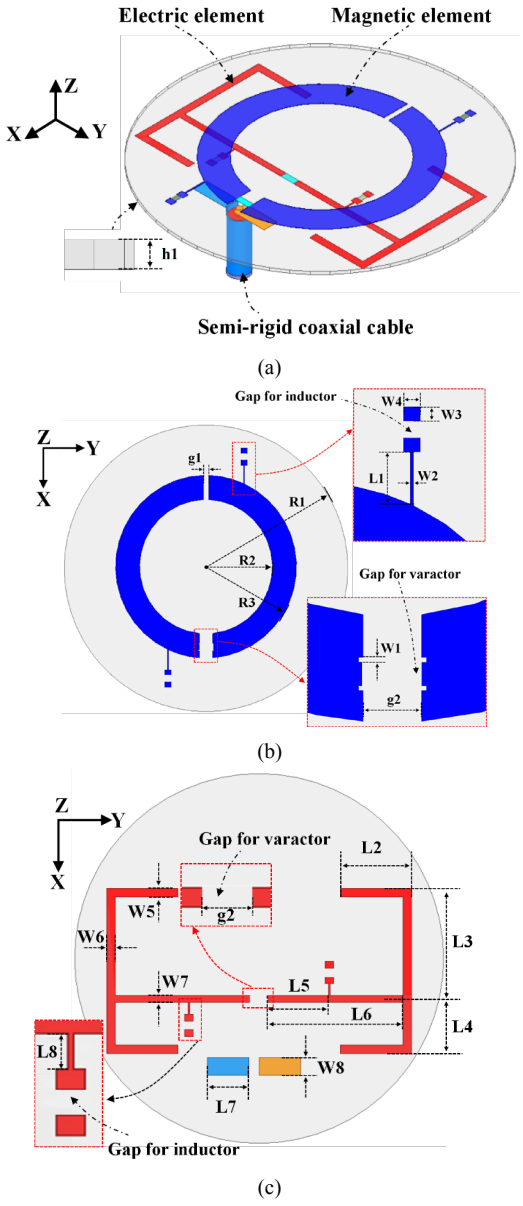

Fig. 1 Configuration of the electrically small, planar, frequency-agile, beam-switchable HDA. (a) 3-D isometric view. (b) Front view. (c) Back view.

As shown in Fig. 1(b), the magnetic element is a CLL with an additional gap. This split ring-shaped structure has an inner radius $R2$ and outer radius $R3$. It lies on the xy-plane and is printed and centered on the upper surface of the substrate. The two gaps in this copper ring have different lengths, i.e., $g1 \neq g2$. The gap with length $g2$ accommodates one of the varactor diodes. The currents induced on this CLL element produce the LP field of a magnetic dipole that is oriented along the z-axis.

The electric element is shown in Fig. 1(c). It is an off-centered EAD printed on the lower surface of the substrate. The main body of the EAD consists of two long straight copper strips with the same size $L6 \times W7$ along the y-axis. A gap of length $g2$ is introduced into it to accommodate the second varactor diode. A x-oriented copper strip of length, $L3+L4$, is placed at each end of the long copper strips and orthogonal to them. Both strips are located 5.8 mm away from the center of the substrate. Four small copper strips with the

same length, *L2*, extend along the *y*-axis from the ends of these two *x*-oriented strips. The EAD element produces the LP field of an electrical dipole oriented along the *y*-axis.

The CLL and EAD structures operate as NFRP elements that are excited by a coax-fed dipole element. This dipole consists of two isolated copper strips with the same length and width, *L7*×*W8*, also etched on the lower surface of the substrate. To ensure the mechanical stability of the antenna system during its assembly and testing processes, a KTG 141–50 type, semi-rigid, 50-Ω coaxial cable was selected to feed the dipole element. As shown in Fig. 1(a), this 50-Ω coaxial cable is connected and oriented perpendicular to the substrate, and its center and external conductors are, respectively, connected to the two strips of the driven element.

TABLE I.
OPTIMIZED DESIGN PARAMETERS OF THE PLANAR, ELECTRICALLY SMALL, FREQUENCY-AGILE, BEAM-SWITCHABLE HUYGENS DIPOLE ANTENNA (IN MILLIMETERS)

h1 = 0.508	*R1 = 26.5*	*R2 = 12.4*	*R3 = 16.9*	*L1 = 3.4*
L2 = 10.2	*L3 = 15.85*	*L4 = 7.85*	*L5 = 9.4*	*L6 = 20.05*
L7 = 5.8	*L8 = 3.8*	*W1= 0.2*	*W2 = 0.2*	*W3 = 1.0*
W4 = 1.2	*W5 = 1.2*	*W6 = 1.2*	*W7 = 1.0*	*W8 = 2.5*
g1 = 0.9	*g2 = 1.2*	*Null*		

A. Tailored Aspects of the Design

Several design details tailored for the desired performance characteristics must be elucidated. The presence of the additional gap in each of the NFRP elements ensures a proper accommodation of the varactor diode and its bias circuit into their structures. While the presence of the varactors allows them to operate normally as they would without the gap, they also help accomplish the electrically smaller size of the entire system by introducing more capacitance into each element and, hence, lowering its resonance frequency.

Notice that two copper strips with dimensions *L1*×*W2* extend along the *x*-axis from each NFRP element. Two pairs of copper patches with dimensions *W3*×*W4* are also present. Each strip is connected to the nearest patch. Two 8.7 nH coil inductors (LQW18A from Murata) were installed across the pads of each NFRP element to block any RF signals from entering the DC bias network. The outside patch of each pair is employed as the connection point for the external DC feeder lines required to control each varactor's capacitance value.

Note also that the typical EAD NFRP elements introduced, for example, in [12], [14], [15] are symmetric structures. In contrast, the EAD NFRP element is asymmetric in this design, i.e., the pair of copper strips that constitute the *x*-oriented end pieces of the EAD have different lengths, i.e., $L3 \neq L4$. Our simulation studies identified that the asymmetric EAD NFRP element helped reduce the radius of the substrate without negatively impacting the system's performance. In particular, by optimizing its design parameters, the required balance between the electric and magnetic NFRP elements to attain the desired Huygens dipole performance was achieved over the entire frequency-agile range.

Two Skyworks Green SMV2019 SC-79 varactor diodes were selected for this design in order to realize the frequency-agile, beam-switchable radiation performance. According to its datasheet, the equivalent circuit model of the varactor diode is simply a RLC series combination with an inductance of 0.7 nH and a resistance of 4.8 Ω [20]. Each one has a junction capacitance that changes in the range from 0.3 to 2.22 pF when its reversed bias voltage is varied from 20 to 0 V [20]. In order to ensure the proper positioning of the varactor diode in the larger CLL element during assembly of the prototype, two small rectangular slots were etched on both sides of its varactor diode gap as markers. They were *W1*×*W1* in size. These values were used in the simulations to optimize the design and its performance.

B. Design Principles

According to the existing HDA design principles [5], a broadside radiating HDA can be obtained when its magnetic and electric NFRP elements are perpendicularly oriented; have balanced radiated fields, i.e., radiated electric and magnetic fields with the same magnitudes; and have overlapping phase centers. The requisite fields arise from balanced in-phase current moments, which physically means a ±90º phase difference between the actual $\underline{\underline{J}}$ and $\underline{\underline{K}}$ current densities induced, respectively, on its electric and magnetic elements. The unidirectional beam emitted by an HDA is directed broadside to those NFRP elements. Its cardioid pattern is identical in both principal planes. The specific broadside direction is determined by sign of those currents according to the right-hand rule, $\underline{\underline{J}} \times \underline{\underline{K}}$.

As illustrated in Fig. 2, the true current directions are represented by the dashed straight red arrows on the electric NFRP element (same as $\underline{\underline{J}}$) and by the dashed curved blue arrows on the magnetic one ($\underline{\underline{K}}$ obtained then by the right hand rule). The maximum beam direction for the HDA system shown in Fig. 1 is along the +*x*-axis or the -*x*-axis when the phase of the currents on either the electric or magnetic dipole element are changed by 180º.

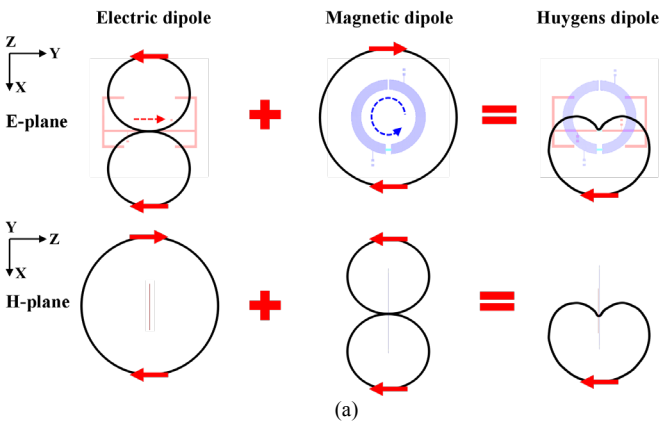

(a)

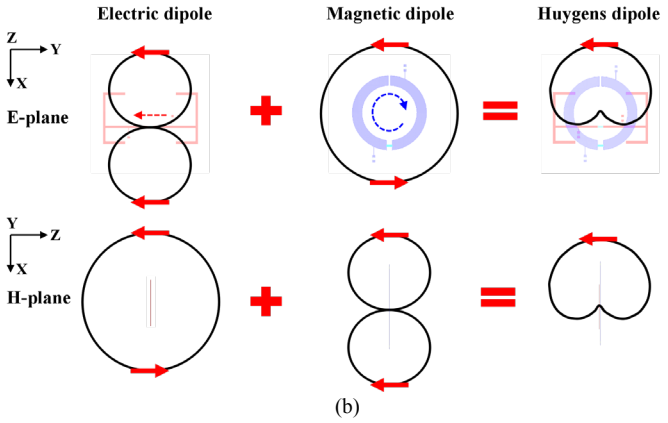

Fig. 2 Design concept of the electrically small, planar, frequency-agile, beam-switchable HDA. (a) Radiating along the +*x*-axis. (b) Radiating along the -*x*-axis.

The capacitance values of the varactor diodes in the magnetic and electric NFRP elements in this design are represented, respectively, by C_m and C_e. The C_m and C_e values are determined with the following design guidelines. As a first step, one would set the values of C_m and C_e near the middle value of the available varactor diodes. As a second step, the HDA's operational performance characteristics are then optimized for these fixed C_m and C_e values by changing the electric and magnetic NFRP elements' dimensions, the distance between them, and the size of the driven element. In our design, we first considered the system to be radiating along the -*x*-axis. We then considered its performance along the +*x*-axis and found that it can be obtained mainly by decreasing the value of C_e. With the determined most suitable sizes of the magnetic and electric NFRP elements, the third step is an evaluation one in which one simultaneously increases/decreases the capacitance values C_m and C_e to explore the frequency agility range of the system while maintaining the desired Huygens radiation behavior. If the desired frequency band is not covered, different varactors can be selected and the system re-optimized. Because the phases of the magnetic and electric elements vary with the values of C_m and C_e, the main beam directions are easily switched at the same time as the resonance frequency is.

The specific C_m and C_e values that realize the two unidirectional endfire states, State A and State B, of the antenna are represented as the frequency-agile (ball) markers in Figs. 3(a) and 3(b), respectively. In particular, the simulated frequency-agile range of the antenna in State A is 1.472–1.55 GHz when C_m (C_e) is varied from 0.54 (1.06) to 0.84 (1.1) pF. The antenna generates a Huygens radiation pattern whose maximum is directed along the +*x*-axis. In contrast, State B is obtained with a different range of capacitance values on the EAD element. By changing C_m (C_e) from 0.575 (0.92) to 0.9 (0.985) pF, the frequency-agile range of the antenna remains essentially the same, 1.473–1.551 GHz, but the unidirectional Huygens radiation pattern has its maximum now directed along the -*x*-axis.

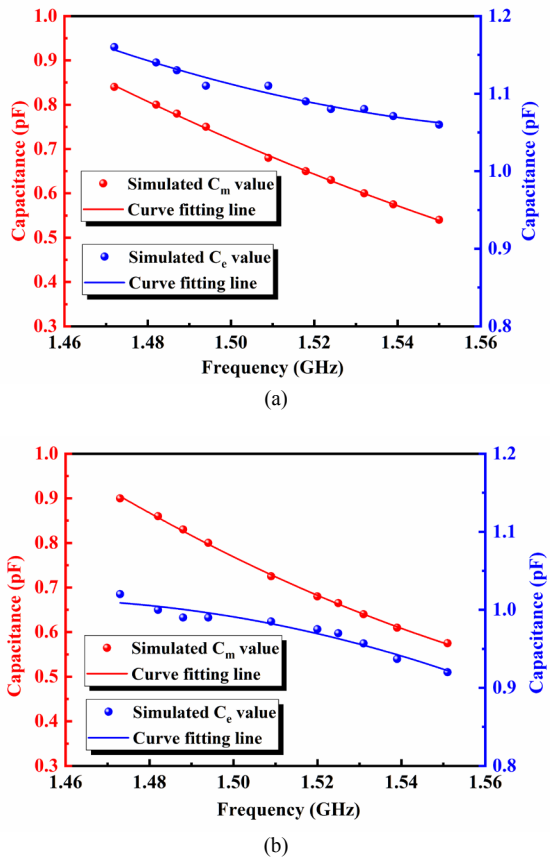

Fig. 3 The relationship between the discrete capacitance values C_m and C_e, and their curve-fit lines as functions of the resonance frequency f_{res}. (a) State A. (b) State B.

As shown in Fig. 3, a curve fitting line was determined in order to obtain the values of C_m and C_e corresponding to all of the resonance frequencies in the frequency-agile range in both State A and State B. The second-order polynomial equation: $C(f_{res}) = a_0 + a_1 \times f_{res} + a_2 \times f_{res}^2$, was used to curve fit the discrete values of C_m and C_e. The calculations of the coefficients a_0, a_1, and a_2 for each state were carried out using the curve fitting tools in MATLAB R2017a. The subsequent equations of the curves that fit the C_m and C_e values in State A were:

$$\begin{cases} C_m(f_{res}) = 26.83 - 30.71 \times f_{res} + 8.87 \times f_{res}^2 \\ C_e(f_{res}) = 19.98 - 23.79 \times f_{res} + 7.47 \times f_{res}^2 \end{cases} \quad (1)$$

where $C_m(f_{res})$ and $C_e(f_{res})$ represent, respectively, the capacitance values of the varactor in the magnetic and electric NFRP element at the resonance frequency f_{res}. The main beam points along the +*x*-axis, when $C_m(f_{res})$ and $C_e(f_{res})$ satisfy these relations over the frequency range from 1.472 to 1.55 GHz.

Similarly, the curve-fit equations of the C_m and C_e values in State B were determined to be:

$$\begin{cases} C_m(f_{res}) = 41.99 - 50.34 \times f_{res} + 15.24 \times f_{res}^2 \\ C_e(f_{res}) = -17.53 + 25.60 \times f_{res} - 8.83 \times f_{res}^2 \end{cases} \quad (2)$$

The main beam points along the -*x*-axis when $C_m(f_{res})$ and $C_e(f_{res})$ satisfy these relations over the frequency range from 1.473 to 1.551 GHz.

C. Parameter studies

Studies of the two major design parameters are provided to illustrate the optimization guidelines. Simulations are performed keeping all but one of the design parameters fixed. For example, when setting C_m = 0.725 pF and C_e = 0.985 pF, the antenna operates in State B. Figs. 4 and 5 present the effects on the $|S_{11}|$, realized gain and FTBR values when the radius of the magnetic NFRP element (*R2*) and the length of the electric NFRP element (*L6*) are changed. As Fig. 4 illustrates, the resonance frequency is greatly impacted when *R2* changes. Similarly, the realized gain and FTBR values witness corresponding changes. When *L6* is changed, Fig. 5 indicates that while the resonance frequency, realized gain and FTBR values are affected, the variations are not as large. These parameter studies confirm that the magnetic NFRP element size plays a primary role in determining the resonance frequency and that the electric NFRP element provides a means to fine tune it and the overall radiation performance characteristics.

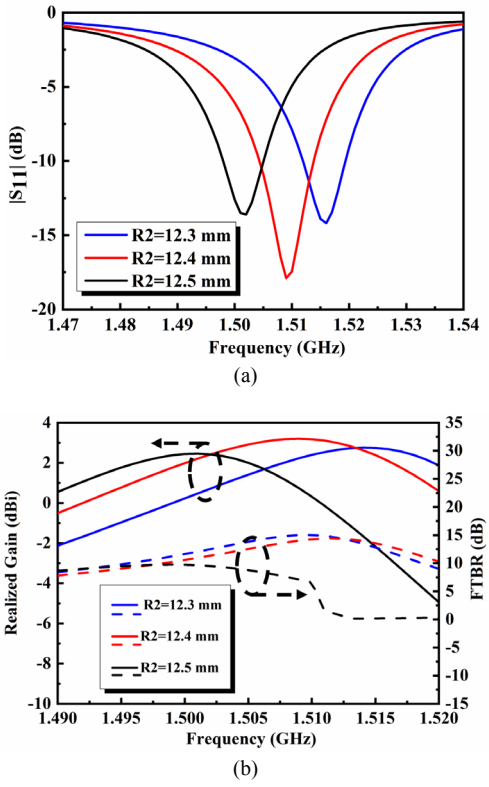

Fig. 4 The effects of changing the magnetic dipole radius *R2* on the performance characteristics of the electrically small, planar, the frequency-agile, beam-switchable HDA. (a) The $|S_{11}|$ (reflection coefficient) values. (b) The realized gain and FTBR values.

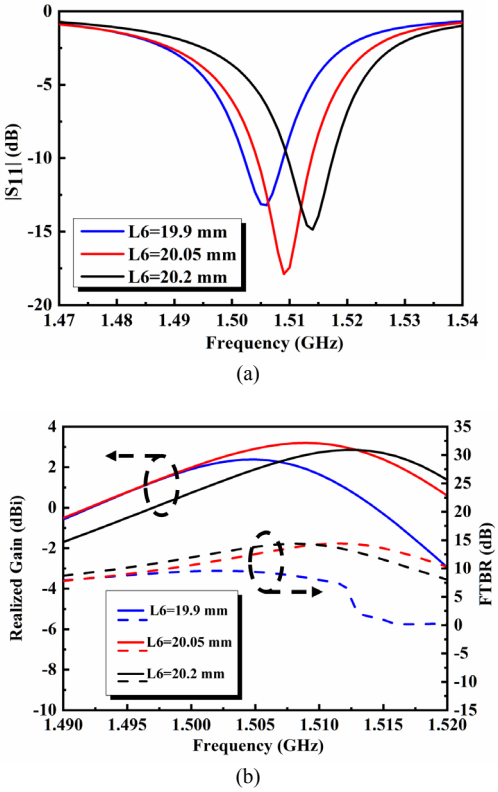

Fig. 5 The effects of changing the electric dipole length *L6* on the performance characteristics of the electrically small, planar, frequency-agile, beam-switchable HDA. (a) The $|S_{11}|$ (reflection coefficient) values. (b) The realized gain and FTBR values.

III. Simulated and Measured Results

The optimized electrically small, frequency-agile, beam-switchable HDA design was fabricated, assembled, and measured. The prototype is shown in Fig. 6(a), which includes the fabricated antenna and a 50.7 mm-long sleeve balun (~0.25 λ_0) introduced only for measurement purposes, it is not included in the calculation of the *ka* value of the system. The balun was necessary to mitigate any spurious currents induced on the outer walls of the long measurement coax cable. It ensured the accuracy of the measurements of the impedance matching and of the far-field directivity pattern characteristics [21], [22].

As shown in Fig. 6(b), two pairs of DC bias lines were used to tune the value of the varactor diodes, i.e., $V_m(+)$ and $V_m(-)$ to control the C_m value, and $V_e(+)$ and $V_e(-)$ to control the C_e value. The $|S_{11}|$ values of the fabricated antenna were measured with an Agilent E8361A PNA Vector Network Analyzer (VNA) and two voltage-stabilized sources. The far-field realized gain (RG) patterns and radiation efficiency (RE) were measured with an SG128 multi-probe antenna measurement system at the China Academy of Information and Communications Technology, Chongqing, China [23]. The antenna under test (AUT) in the measurement chamber is shown in Fig. 6(c).

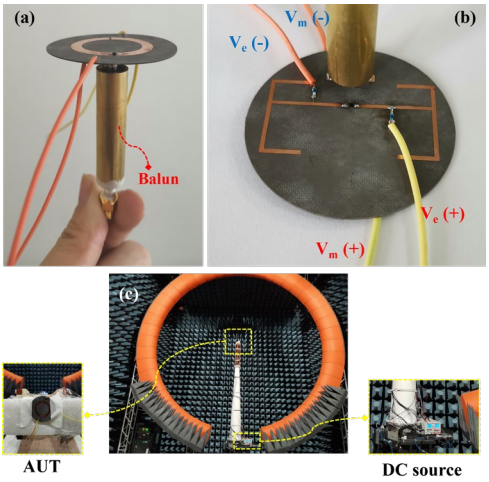

Fig. 6 Fabricated prototype of the electrically small, planar, frequency-agile, beam-switchable HDA. (a) Side view of the assembled antenna. (b) Bottom view of the assembled antenna. (c) The AUT in the multi-probe anechoic chamber.

A. Results and Performance

The measured $|S_{11}|$ results for State A and State B, together with their simulated values (taking into account of the presence of the balun), are presented in Figs. 7 and 8, respectively. Note that the capacitances of the varactor diodes used in the simulations were the values that occur for the bias voltage values applied in the experiments. We selected only five cases to verify the prototypes frequency-agile ability.

The simulated and measured $|S_{11}|$ values for State A are presented in Figs. 7(a) and (b), respectively. When the bias DC voltage V_m (V_e) was set to: 3.8 (1.6), 4.2 (1.7), 4.9 (2.0), 5.4 (2.1) and 6.0 (2.5) V, the corresponding resonant frequencies were 1.474, 1.488, 1.509, 1.524 and 1.55 GHz, respectively. The associated $|S_{11}|_{min}$ values were -13.0, -12.9, -11.9, -10.6 and -10.5 dB. Fig. 7 clearly indicates that the resonance frequencies increase with a decrease in the C_m and C_e values. When the values of C_m (V_m) and C_e (V_e) were changed from 0.84 pF (3.8 V) to 0.54 pF (6.0 V) and from 1.1 pF (1.6 V) to 1.06 pF (2.5 V), the simulated (measured) resonance frequencies increased from 1.472 (1.474) to 1.55 (1.55) GHz, yielding a tunable bandwidth of 78 (76) MHz, i.e., a 5.1% (5.0%) tunable fractional bandwidth. The simulated and measured FTBR values are higher than 6.81 and 5.61 dB, respectively, for each of these State A cases.

The simulated and measured $|S_{11}|$ results for State B are similarly presented in Figs. 8(a) and (b). When the bias DC voltage V_m (V_e) was set to: 3.5 (2.9), 4.0 (3.0), 4.5 (3.0), 5.0 (3.1) and 5.4 (3.4) V, the corresponding resonance frequencies were 1.473, 1.49, 1.511, 1.526 and 1.55 GHz, respectively. The associated $|S_{11}|_{min}$ values were -21.4, -33.1, -14.4, -11.1 and -10.3 dB. When the values of C_m (V_m) and C_e (V_e) were changed from 0.9 pF (3.5 V) to 0.575 pF (5.4 V) and from 1.02 pF (2.9 V) to 0.92 pF (3.4 V), the simulated (measured) resonance frequencies increased from 1.473 (1.473) to 1.551 (1.55) GHz, yielding a tunable bandwidth of 0.078 (0.077) GHz, i.e., a 5.1% (5.1%) tunable fractional bandwidth. The simulated and measured FTBR values are higher than 6.4 and 5.97 dB, respectively, for each of these State B cases.

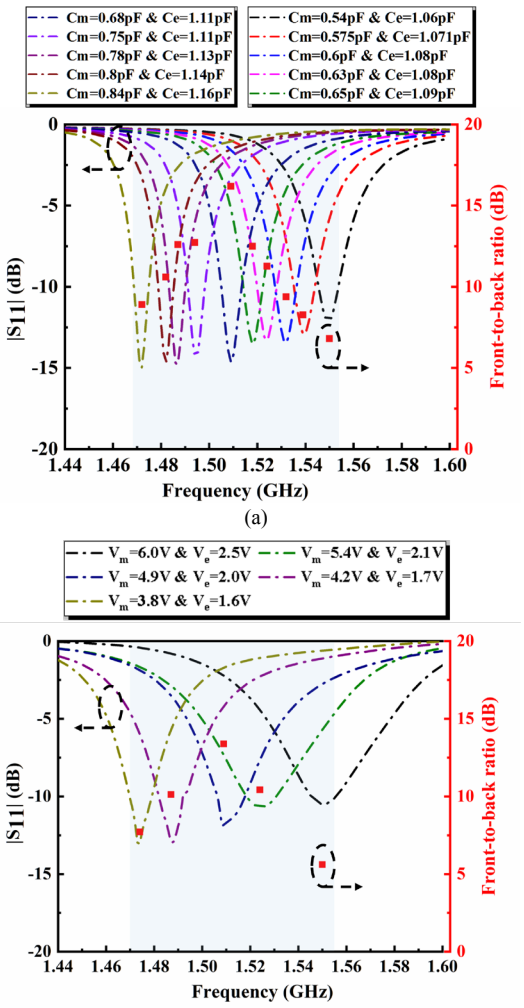

Fig. 7 Simulated and measured $|S_{11}|$ values of the electrically small, planar, frequency-agile, beam-switchable HDA in State A. (a) Simulated $|S_{11}|$ values. (b) Measured $|S_{11}|$ values.

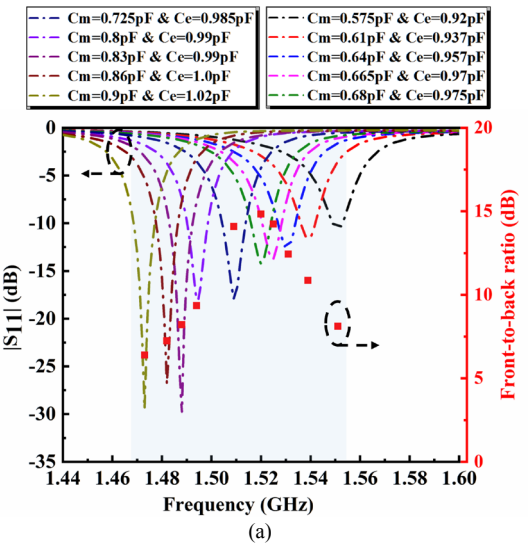

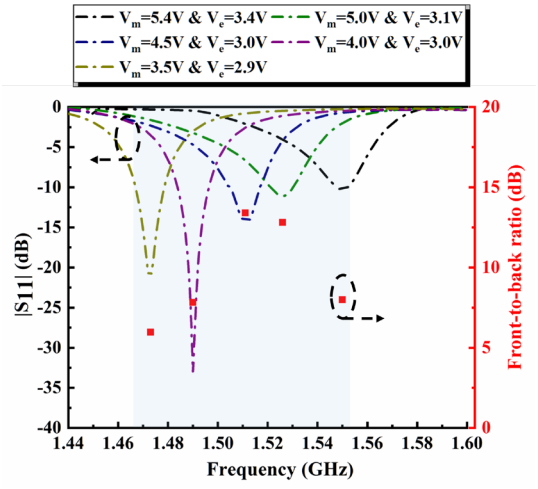

(b)

Fig. 8 Simulated and measured $|S_{11}|$ values of the electrically small, planar, frequency-agile, beam-switchable HDA in State B. (a) Simulated $|S_{11}|$ values. (b) Measured $|S_{11}|$ values.

In general, these measured results are in good agreement with their simulated values. The measured frequency-agile range of States A and B were from 1.474 to 1.55 GHz and from 1.473 to 1.55 GHz, respectively. These results confirm that the frequency-agile range of the two oppositely directed states are virtually the same. The corresponding simulated (measured) electrical size of the system at the highest resonance frequency $f_{high,\ sim.}$ = 1.55 GHz ($f_{high,\ meas.}$ = 1.55 GHz) within the measured frequency agility range is ka_{high} = 0.86 (0.86).

The measured and simulated realized gain (RG) patterns for States A and B are compared in Figs. 9 and 10, respectively. The realized gain patterns were measured in each beam state for the same five resonance frequencies.

The measurements confirmed that the antenna generates a Huygens dipole pattern whose maximum is directed along the +*x*-axis in State A. Figs. 9(a)-(e) show the simulated (measured) realized gain patterns when its operating frequency is tuned to 1.472 (1.474), 1.487 (1.488), 1.509 (1.509), 1.525 (1.524) and 1.55 (1.55) GHz, respectively. The co-polar and cross-polar patterns are shown for each orthogonal cut-plane. They confirm that the antenna achieved good stable, endfire Huygens radiation performance across the entire frequency-agile range. The antenna achieved simulated (measured) peak RG values of 2.46 (2.21), 2.88 (2.68), 3.13 (2.91), 2.83 (2.53), and 2.31 (2.21) dBi at 1.472 (1.474), 1.487 (1.488), 1.509 (1.509), 1.525 (1.524) and 1.55 (1.55) GHz, respectively. The corresponding simulated (measured) FTBR values are 8.9 (7.71), 12.6 (10.12), 16.18 (13.38), 11.27 (10.43), and 6.81 (5.61) dB. The associated cross-polarized levels are much smaller in comparison.

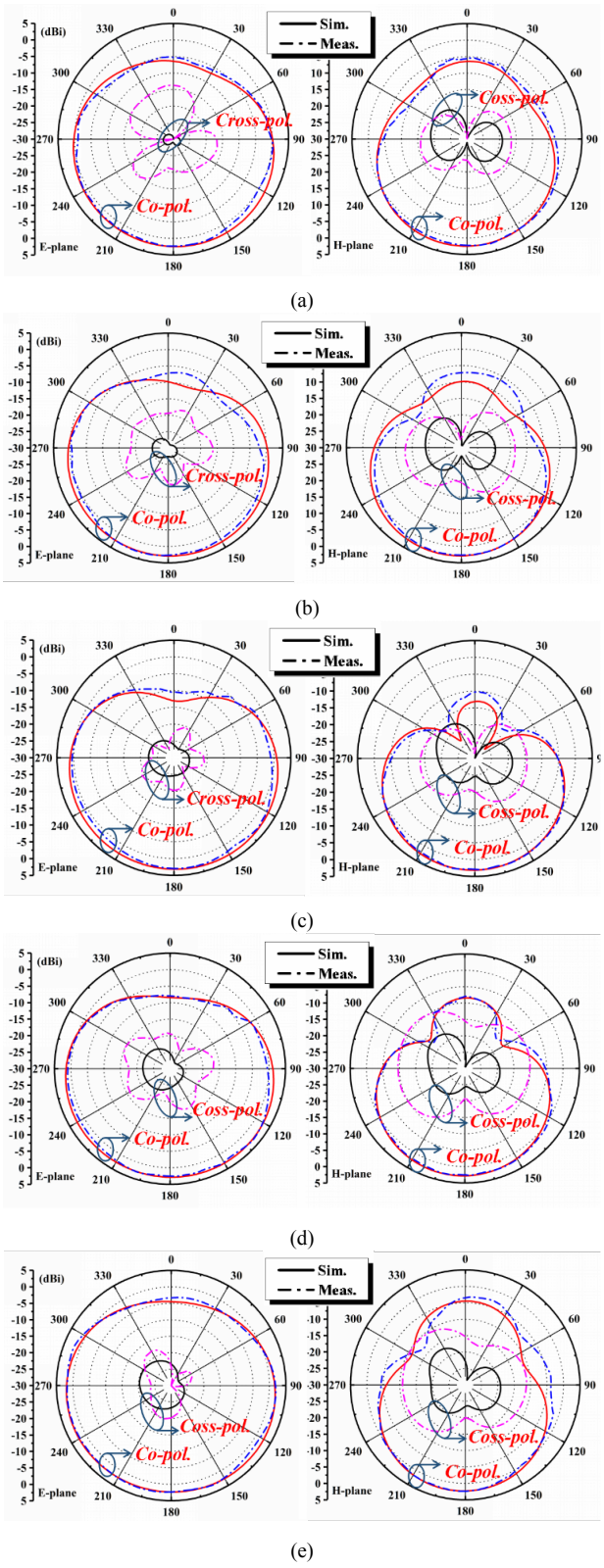

(a)

(b)

(c)

(d)

(e)

Fig. 9 Simulated and measured realized gain patterns of the developed ESA at the simulated (measured) resonance frequencies in State A. (a) 1.472 (1.474) GHz. (b) 1.487 (1.488) GHz. (c) 1.509 (1.509) GHz. (d) 1.525 (1.524) GHz. (e) 1.55 (1.55) GHz.

Similarly, the antenna generates a Huygens dipole patterns whose maxima are directed along the -*x*-axis in State B. Figs.

10(a)-(e) show the simulated and measured realized gain patterns. The antenna achieves simulated (measured) peak RG values of 2.52 (2.37), 2.86 (2.52), 3.19 (2.92), 2.89 (2.68), and 2.10 (1.99) dBi at 1.473 (1.473), 1.488 (1.49), 1.509 (1.511), 1.525 (1.526) and 1.551 (1.55) GHz, respectively. The corresponding simulated (measured) FTBR values are 6.4 (5.97), 8.21 (7.82), 14.09 (13.4), 14.23 (12.81), and 8.11 (7.99) dB. These results confirm that stable, antipodal endfire Huygens radiation performance was obtained when the pre-determined DC voltages were applied to the varactors in both NFRP elements. Again, the associated cross-polarized levels are much smaller in comparison to the corresponding co-polarized values.

The simulated and measured RE values in State A and State B are higher than 70.5% and 67.7% for all of the resonance frequencies in the antenna's frequency-agile range. The simulated and measured radiation patterns for States A and B have 3-dB beamwidths in the E-plane that are larger than those in the H-plane, as observed in Figs. 9 and 10. The main reason for this phenomenon is that when the C_m and C_e values are varied, only the excitation phases of the NFRP elements are changed. Their variation does not also adjust the excitation magnitudes. Thus, when the Huygens radiation effect is formed within the frequency-agile range, the phase differences between the magnetic and electric NFRP elements can be tailored to a desired value at each operating frequency, but their magnitude ratio cannot be.

The simulated and measured values of the prototype in both State A and State B are summarized in Table II for easy comparison. It is noted that the antenna has high RG, FTBR, and RE values in both states over the entire frequency-agile range of the antenna. All of the measured results are basically in good agreement with their simulated values. The relatively small differences between some of them have been considered in simulations and have been found to be due to small fabrication and assembly errors. On the one hand, errors are associated with the fact that the length of the balun and its relative position on the coaxial line were determined manually during the assembly of the system and its insertion into the test range fixtures. Consequently, the balun did not completely remove all of the surface currents on the outer conductor of the coaxial line during the measurements as expected. These assembly issues led to the majority of the differences between the measured and simulated impedance matching levels. On the other hand, the bias lines used during the measurements of the functions of the system also slightly affected the performance characteristics of the antenna. They were not included in the simulations. Our measurement experiences found that their impact was minimized (but not entirely removed) by orienting them orthogonally to the polarization direction of the antenna. Since that the latter is along the *y*-axis, the bias lines of both the magnetic and electric NFRP elements were placed most effectively along the *x*-axis and *z*-axis, respectively. The associated effects nevertheless caused the measured resonances to not be precisely matched to their simulated ones. Finally, fabrication tolerances led to inevitable variations in the design parameters which also led to some of the small measurement and simulation differences.

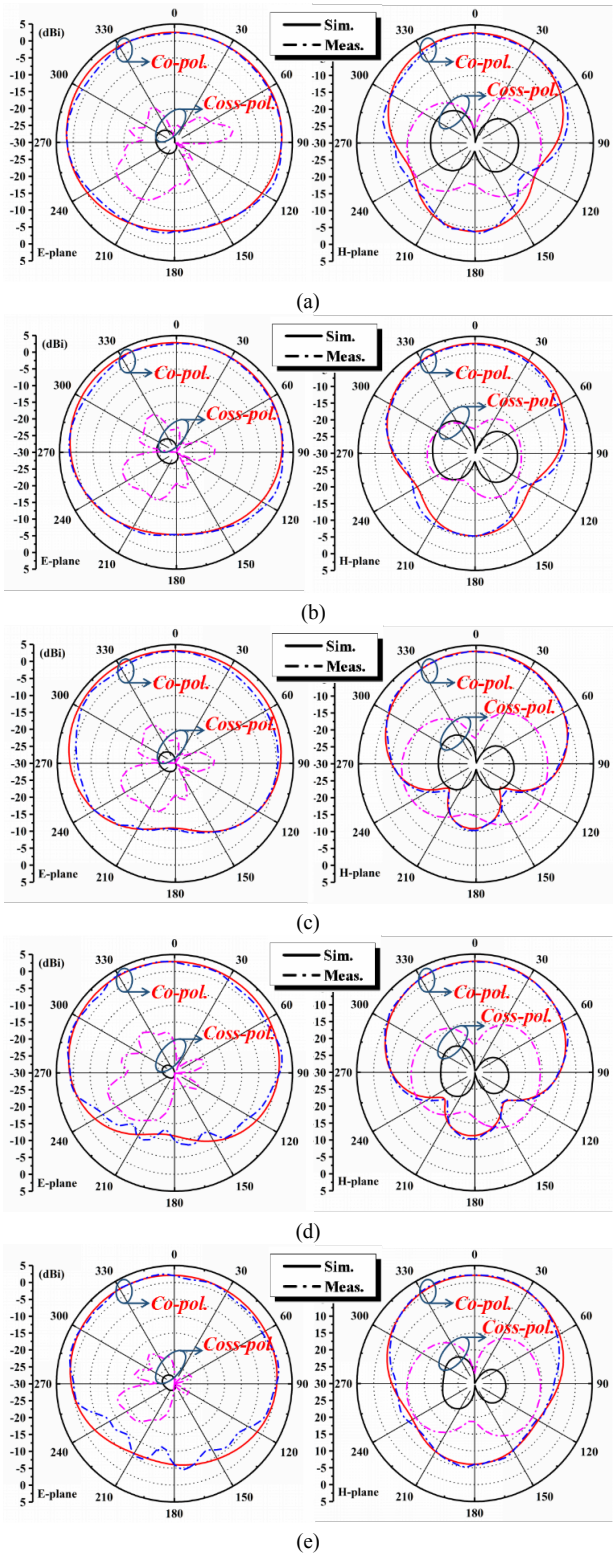

Fig. 10 Simulated and measured realized gain patterns of the developed ESA at the simulated (measured) resonance frequencies in State B. (a) 1.473 (1.473) GHz. (b) 1.488 (1.49) GHz. (c) 1.509 (1.511) GHz. (d) 1.525 (1.526) GHz. (e) 1.551 (1.55) GHz.

TABLE II
SIMULATED (CLEAR) AND MEASURED (SHADED) RESULTS FOR DIFFERENT APPLIED BIAS VOLTAGES

(a) State A

DC voltage (V)	V_m=3.8 V_e=1.6	V_m=4.2 V_e=1.7	V_m=4.9 V_e=2.0	V_m=5.4 V_e=2.1	V_m=6.0 V_e=2.5
Resonance Frequency (GHz)	1.472	1.487	1.509	1.525	1.55
	1.474	1.488	1.509	1.524	1.55
Instantaneous Bandwidth (%)	0.41	0.47	0.59	0.59	0.52
	0.54	0.53	0.66	0.7	0.58
Peak Realized Gain (dBi)	2.46	2.88	3.13	2.83	2.31
	2.21	2.68	2.91	2.53	2.21
FTBR (dB)	8.9	12.6	16.18	11.27	6.81
	7.71	10.12	13.38	10.43	5.61
RE (%)	75	77.2	81.4	82.9	86.1
	67.7	72.2	76.3	77.1%	79.4
3-dB beam coverage in the E-plane	-78° ~ 83°	-82° ~ 87°	-79° ~ 83°	-67° ~ 75°	-51° ~ 60°
	-95.5° ~ 87.5°	-98.5° ~ 100.5°	-80° ~ 100°	-68° ~ 90°	-48.5° ~ 64.5°
3-dB beam coverage in the H-plane	-115° ~ 121°	-115° ~ 121°	-117° ~ 125°	-119° ~ 127°	-122° ~ 129°
	-112.5° ~ 109°	-126.5° ~ 125.5°	-115.5° ~ 120°	-113° ~ 117.5°	-118° ~ 128.5°

(b) State B

DC voltage (V)	V_m=3.5 V_e=2.9	V_m=4.0 V_e=3.0	V_m=4.5 V_e=3.0	V_m=5.0 V_e=3.1	V_m=5.4 V_e=3.4
Resonace Frequency (GHz)	1.473	1.488	1.509	1.525	1.551
	1.473	1.49	1.511	1.526	1.55
Instantaneous Bandwidth (%)	0.61	0.67	0.59	0.52	0.25
	0.74	0.8	0.66	0.52	0.26
Peak Realized Gain (dBi)	2.52	2.86	3.19	2.89	2.10
	2.37	2.52	2.92	2.68	1.99
FTBR (dB)	6.4	8.21	14.09	14.23	8.11
	5.97	7.82	13.4	12.81	7.99
RE (%)	84.6	85.2	82.7	79.1	76.4
	80.4	82.0	80.2	73.6	70.5
3-dB beam coverage in the E-plane	-123° to 126	-114° to 116°	-101° to 103°	-101° ~ 104°	-106° ~ 112°
	-115.5° ~ 131.5°	-116° ~ 131.5°	-80° ~ 100°	-103° ~ 97°	-101.5° ~ 105.5°
3-dB beam coverage in the H-plane	-54° ~ 57°	-55° ~ 58°	-57° ~ 59°	-57° ~ 59°	-57° ~ 60°
	-42.5° ~ 67.5°	-54.5° ~ 50.5°	-61° ~ 64.5°	-62.5° ~ 67°	-55.5° ~ 56°

B. Operating Mechanisms Revisited

The operating mechanisms behind the pattern-switchable states can be further understood and confirmed by the surface current distributions on the main surfaces of the driven and NFRP elements of the antenna. Those obtained from the simulations of State A and State B are shown in Figs. 11 and 12, respectively. They are presented for one period T associated with the resonance frequency point, 1.509 GHz, at the times: t = 0 (marked as a), T/4 (marked as b), T/2 (marked as c) and 3T/4 (marked as d). It is a resonance frequency of both State A and State B. To help understand these current behaviors, their principal directions are highlighted with the additional solid red arrows in Figs. 11 and 12.

Referring to the analysis of the current and field behaviors of the electrically small HDA reported in [12], the fields radiated by the NFPR elements must be in-phase over the entire period T to achieve the Huygens cardioid radiation pattern. As a consequence, the currents on the magnetic NFRP element must be 90º ahead of those on the electric NFRP element. Therefore, the maximum of the unidirectional fields radiated by the currents depicted in Fig. 11 for State A is directed along the +*x*-axis [24], [25] in agreement with the design principles illustrated in Fig. 2(a). In the same manner, the current distribution directions depicted in Fig. 12 for State B agree with those illustrated in Fig. 2(b). Therefore, the maximum of the unidirectional fields radiated by them is directed along the -*x*-axis.

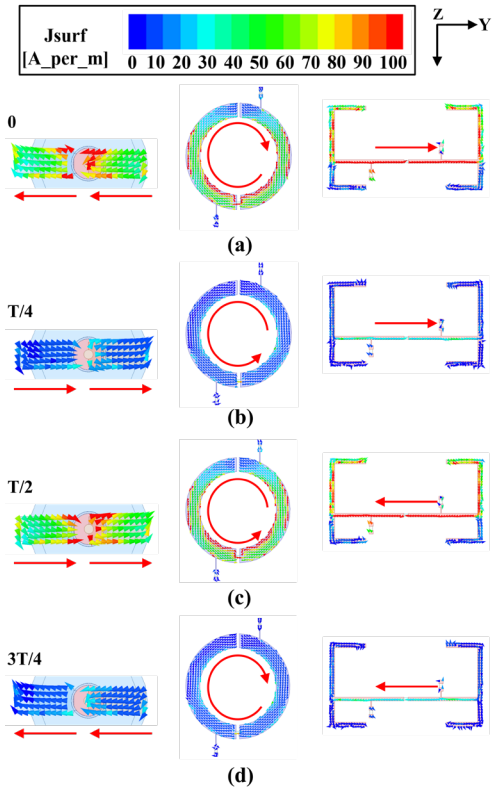

Fig. 11 Surface current distributions on the driven element and on the magnetic and electric NFRP elements at quarter period intervals when the antenna is in its State A.

Table III
COMPARISON OF THE DEVELOPED HDA WITH RELATED FREQUENCY-AGILE AND/OR PATTERN-SWITCHABLE RECONFIGURABLE ANTENNAS REPORTED IN THE LITERATURE*

Ref.	ka_{low}	Type of Reconfigurability	FBW (%)	RG (dBi)	FTBR (dB)	RE (%)	Switch No.	Beam Scanning Capability	Electrical Size (λ_{low}^3)	Configuration
[14]	0.98	Pattern-switchable	1.32	5.4	13.3	85	2	0° & 180°	$\pi \times (0.15)^2 \times 0.0026 = 1.84 \times 10^{-4}$	2-D
[17]	0.34	Frequency-agile	64.6	-0.13~5.04	-	-	3	no	$0.076 \times 0.076 \times 0.023 = 1.33 \times 10^{-4}$	3-D
[26]	0.6	Pattern-switchable	2.7	8.5	7	89.8	2	0° & 180°	$0.12 \times 0.095 \times 0.095 = 1.08 \times 10^{-3}$	3-D
[27]	1.32	Pattern-switchable	15	3.5	25.5	83	4	Full azimuth	$0.41 \times 0.41 \times 0.022 = 3.70 \times 10^{-3}$	2-D
[28]	4.02	Frequency-agile & Pattern-switchable	26.4	5.0	-	-	25	-30°~30°	$0.90 \times 0.90 \times 0.04 = 3.24 \times 10^{-2}$	2-D
[29]	4.59	Frequency agile & Pattern-switchable	30	7.4~10	-	-	40	Full azimuth	$1.19 \times 0.85 \times 0.85 = 8.6 \times 10^{-1}$	3-D
This work	0.81	Frequency-agile & Pattern-switchable	5	2.1~3.19	5.61~13.4	>67.7	2	0° & 180°	$\pi \times (0.13)^2 \times 0.0025 = 1.32 \times 10^{-4}$	2-D

*The 2-D or 3-D designation in the "Configuration" column indicates that the antenna is either planar or volumetric, respectively.

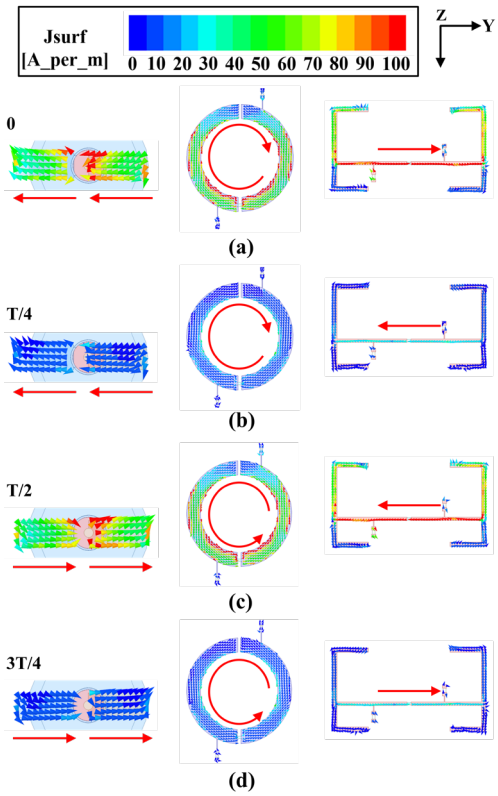

Fig. 12 Surface current distributions on the driven element and on the magnetic and electric NFRP elements at quarter period intervals when the antenna is in its State B.

Comparing the current distributions on the magnetic and electric NFRP elements in State A with those in State B, the changes in the C_m and C_e values that occur to realize State B cause the phase of the currents on the magnetic dipole to advance by $\pi/2$ and the phase of the currents on the electric dipole to retard by $\pi/2$. Therefore, the relative orientations of the currents on the NFRP element are reversed and the Huygens cardioid radiation pattern whose maximum is along the antipodal direction, i.e., the $-x$-axis, is obtained.

A comprehensive comparison is given in Table III. It emphasizes that our planar, frequency-agile, beam-switchable HDA is simpler and electrically smaller with improved functionality in comparison to other recently reported frequency-agile and/or pattern-switchable reconfigurable antennas. The listed performance characteristics include the electrical sizes, bandwidths, RG values, FTBR values, RE values, numbers of diodes employed, beam scanning capability, type of reconfigurability and configuration performance characteristics. Note that the electrical sizes are specified by the lower bound of the operational frequency band, f_{low}, and, hence, for the largest operational wavelength, λ_{low}.

The antennas reported in [14], [26-27] achieved pattern-switchable performance within narrower bandwidths than our design. While those in [14] and [26] used two p-i-n diodes to achieve only fixed pattern-switchable performance, our antenna uses two varactor diodes to achieve simultaneously both frequency-agile and pattern-switchable functions. The system reported in [27] required four diodes for a pattern-switchable only function. The stated volume of the frequency-agile ESA reported in [17] is comparable to our design. However, in contrast, it was realized with a large ground plane. The reported volume is that of the radiating element alone and, hence, not the entire antenna. Moreover, it required three varactor diodes for its frequency agile, fixed pattern performance.

Both frequency-agile and beam-switchable antennas were reported in [28] and [29]. They were very electrically large with the volumes of those two antennas being $3.24 \times 10^{-2}\ \lambda_{low}^3$ ($ka_{low} = 4.02$) [28] and $8.6 \times 10^{-1}\ \lambda_{low}^3$ ($ka_{low} = 4.59$) [29]. The two functionalities in those designs required 25 and 40 p-i-n diodes, respectively. The beam coverage of the antenna in [28]

was around ±30° in the E-plane with a 26.4% continuous bandwidth tuning range. The beam coverage of the antenna in [29] was 360° in the H-plane with a 30.0% continuous bandwidth tuning range. The volume of our design, 1.32×10^{-4} λ_{low}^{3}, is 245.5 times smaller than that in [28] and 6515.1 × smaller than that in [29]. Furthermore, the physical aperture area of our antenna, 5.3×10^{-2} λ_{low}^{2}, is 15.3 (13.6) times smaller than the one in [28] ([29]). Thus, its peak realized gain being only ~1.81 dB smaller than the antenna in [28] and only ~6.81 dB smaller than the one in [29], is remarkable.

IV. Conclusion

A frequency-agile, beam-switchable electrically small Huygens dipole antenna was presented. The frequency tunability and beam switchability were simultaneously achieved through implementing a varactor diode into each of the NFRP elements. The antenna design and its prototype were realized with a single-layer substrate. By changing the capacitance values of the two varactor diodes, it was demonstrated that this ESA is capable of dynamically achieving two independent antipodal unidirectional endfire radiating states over the same frequency-agile range. The measured results indicate that the prototype exhibits a 5% –10-dB fractional impedance bandwidth; this is more than ten times larger than the 0.46% value of the passive Huygens dipole ESA reported in [12]. To the best of our knowledge, this is the first time that both the frequency tunability and beam switchability have been achieved in an electrically small antenna size. The advantageous performance characteristics of our developed antenna include its electrically small size, good radiation efficiency, and ability to simultaneously change its operating frequency and beam direction while maintaining stable cardioid-shaped directivity patterns. They empower it as an attractive candidate for a variety of wireless applications that require high performance, multifunctional radiating elements to enable current and future, for example, IoT ecosystem concepts.

References

[1] W. Lin, R. W. Ziolkowski, and J. Huang, "Electrically small, low-profile, highly efficient, Huygens dipole rectennas for wirelessly powering Internet-of-Things devices," *IEEE Trans. Antennas Propag.*, vol. 67, no. 6, pp. 3670-3679, Jun. 2019.

[2] S. Lim and H. Ling, "Design of electrically small Yagi antenna," *Electron. Lett.*, vol. 43, no. 5, pp. 3–4, Mar. 2007.

[3] J. Ng and R. W. Ziolkowski, "Combining metamaterial-inspired electrically small antennas with electromagnetic band gap (EBG) structures to achieve higher directivities and bandwidths," in *Proc. 2012 International Workshop on Antenna Technology (iWAT 2012)*, Tucson, America, pp. 189-192, Mar. 2012.

[4] M.-C. Tang and R. W. Ziolkowski, "Efficient, high directivity, large front-to-back-ratio, electrically small, near-field-resonant-parasitic antenna," *IEEE Access*, vol. 1, no. 1, pp. 16 - 28, May 2013.

[5] R. W. Ziolkowski, "Low profile, broadside radiating, electrically small Huygens source antennas," *IEEE Access*, vol. 3, pp. 2644-2651, Dec. 2015.

[6] P. Jin and R. W. Ziolkowski, "Metamaterial-inspired, electrically small Huygens sources," *IEEE Antennas Wirel. Propag. Lett.*, vol. 9, pp. 501-505, 2010.

[7] T. Niemi, P. Alitalo, A. O. Karilainen, and S. A. Tretyakov, "Electrically small Huygens source antenna for linear polarisation," *IET Microw. Antennas Propag.*, vol. 6, no. 7, pp. 735–739, 2012.

[8] W. Lin and R. W. Ziolkowski, "Electrically small Huygens antenna-based fully-integrated wireless power transfer and communication system," *IEEE Access*, vol. 7, pp. 39762-39769, Mar. 2019.

[9] S. Lee, G. Shin, S. M. Radha, J. Choi and I. Yoon, "Low-Profile, electrically small planar Huygens source antenna with an endfire radiation characteristic," *IEEE Antennas Wirel. Propag. Lett.*, vol. 18, no. 3, pp. 412-416, Mar. 2019.

[10] W. Lin and R. W. Ziolkowski, "Electrically-small, low-profile, Huygens circularly polarized antenna," *IEEE Trans. Antennas Propag.*, vol. 66, no. 2, pp. 636-643, Feb. 2018.

[11] P. Alitalo, A. O. Karilainen, T. Niemi, C. R. Simovski, and S. A. Tretyakov, "Design and realisation of an electrically small Huygens source for circular polarisation," *IET Microw. Antennas Propag.*, vol. 5, no. 7, pp. 783–789, 2010.

[12] M.-C. Tang, Z. Wu, T. Shi, H. Zeng, W. Lin, and R. W. Ziolkowski, "Dual-linearly polarized, electrically small, low-profile, broadside radiating, Huygens dipole antenna," *IEEE Trans. Antennas Propag.*, vol. 66, no. 8, pp. 3877–3885, Aug. 2018.

[13] P. F. Hu, Y. M. Pan and B. Hu, "Electrically small, planar, complementary antenna with reconfigurable frequency," *IEEE Trans. Antennas Propag.*, vol. 67, no. 8, pp. 5176-5184, Aug. 2019.

[14] Z. Wu, M.-C. Tang, M. Li, and R. W. Ziolkowski, "Ultralow-profile, electrically small, pattern-reconfigurable metamaterial-inspired Huygens dipole antenna," *IEEE Trans. Antennas Propag.*, vol. 68, no. 3, pp. 1238-1248, Mar. 2020.

[15] M.-C. Tang, T. Shi, and R. W. Ziolkowski, "Electrically small, broadside radiating Huygens source antenna augmented with internal non-Foster elements to increase its bandwidth," *IEEE Antennas Wirel. Propag. Lett.*, vol. 16, pp. 712-715, 2017.

[16] L. M. Feldner, C. T. Rodenbeck, C. G. Christodoulou, and Nicola Kinzie, "Electrically small frequency-agile PIFA-as-a-package for portable wireless devices," *IEEE Trans. Antennas Propag.*, vol. 55, no. 11, pp. 3310-3319, Nov. 2007.

[17] Y. Yu, J. Xiong, H. Li, and S. He, "An electrically small frequency reconfigurable antenna with a wide tuning range," *IEEE Antennas Wirel. Propag. Lett.*, vol. 10, pp. 103-106, 2011.

[18] C. G. Christodoulou, Y. Tawk, S. A. Lane, and S. R. Erwin, "Reconfigurable antennas for wireless and space applications," *Proc. IEEE*, vol. 100, no. 7, pp. 2250–2261, Jul. 2012.

[19] E. H. Lim and K. W. Leung, *Compact Multifunctional Antennas for Wireless Systems*. John Wiley & Sons: Hoboken, New Jersey, USA, 2012.

[20] SMV2019 from Skyworks Green. [Online]. Available: https://www.mouser.cn/datasheet/2/472/SMV2019_to_SMV2023_Series_200074Q-1079512.pdf

[21] S. A. Saario, J. W. Lu, and D. V. Thiel, "Full-wave analysis of choking characteristics of sleeve balun on coaxial cables," *Electron. Lett.*, vol. 38, no. 7, pp. 304–305, Mar. 2002.

[22] C. Icheln, J. Krogerus, and P.Vainikainen, "Use of balun chokes in small-antenna radiation measurements," *IEEE Trans. Antennas Propag.*, vol.53, no. 2, pp. 498-506, Apr. 2004.

[23] SG128 multi-probe antenna measurement system. [Online]. Available: https://www.mvg-world.com/en/system/files/datasheet_sg128_bd.pdf

[24] R. W. Ziolkowski, "Custom-designed electrically small Huygens dipole antennas achieve efficient, directive emissions into air when mounted on a high permittivity block," *IEEE Access*, vol. 7, pp. 163365-163383, Nov. 2019.

[25] A. D. Yaghjian, "Increasing the supergain of electrically small antennas using metamaterials," in *Proc. EuCAP*, Apr. 2009, pp. 858–860.

[26] S. Lim and H. Ling, "Design of electrically small, pattern reconfigurable Yagi antenna," *Electron. Lett.*, vol. 43, no. 24, pp. 1326–1327, Nov. 2007.

[27] J. Ouyang, Y. M. Pan, and S. Y. Zheng, "Center-fed unilateral and pattern reconfigurable planar antennas with slotted ground plane," *IEEE Trans. Antennas Propag.*, vol. 66, no. 10, pp. 5139-5149, Oct. 2018.

[28] F. Costa, A. Monorchio, S. Talarico and F. M. Valeri, "An active high-impedance surface for low-profile tunable and steerable antennas," *IEEE Antennas Wirel. Propag. Lett.*, vol. 7, pp. 676-680, 2008.

[29] C. Gu, S. Gao, B. S.-Izquierdo, E. A. Parker, W. Li, X. Yang, and Z. Cheng, "Frequency-agile beam-switchable antenna," *IEEE Trans. Antennas Propag.*, vol. 65, no. 8, pp. 3819-3826, Aug. 2017.

Zhentian Wu was born in Anhui, China, in 1994. He received the B.S. degree from the West Anhui University, Luan, China, in 2016. He is currently pursuing the Ph.D. degree in electronics and communication engineering in the School of Microelectronics and Communication Engineering, Chongqing University, China.

He current research interests include electrically small antenna and directional antenna and their applications.

Ming-Chun Tang (S'12–M'13–SM'16) received the B. S. degree in physics from the Neijiang Normal University, Neijiang, China, in 2005 and the Ph. D. degree in radio physics from the University of Electronic Science and Technology of China (UESTC), in 2013. From August 2011 to August 2012, he was also with the Department of Electrical and Computer Engineering, The University of Arizona, Tucson, AZ, USA, as a Visiting Scholar. He is currently a full Professor in the School of Microelectronics and Communication Engineering, Chongqing University, China. His research interests include electrically small antennas, RF circuits, metamaterial designs and their applications.

Prof. Tang is the Senior Member of the Chinese Institute of Electronics. He was a recipient of the National Science Fund for Excellent Young Scholars in 2019. He was a recipient of the Best Student Paper Award in the 2010 International Symposium on Signals, Systems and Electronics (ISSSE2010) held in Nanjing, China. His Ph.D. students received Best Student Paper Awards from the IEEE 7th Asia-Pacific Conference on Antennas and Propagation (2018 IEEE APCAP) held in Auckland, New Zealand, 2019 IEEE International Applied Computational Electromagnetics Society (ACES) Symposium held in Nanjing, China, 2019 IEEE International Workshop on Electromagnetics: Applications and Student Innovation Competition held in Qingdao, China, and 2019 Cross Strait Quad-Regional Radio Science and Wireless Technology Conference held in Taiyuan, China. He is the founding Chair of the IEEE AP-S / MTT-S Joint Chongqing Chapter. He serves on the Editorial Boards of several journals, including *IEEE Access*, *Electronics Letters* and *IET Microwaves, Antennas & Propagation*. He has also served on the review boards of various technical journals, and many international conferences as a General Chair, TPC Member, Session Organizer, and the Session Chair.

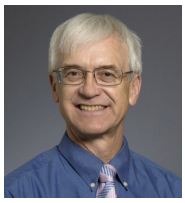

Richard W. Ziolkowski (M'87–SM'91–F'94-LF'20) received the Sc. B. (*magna cum laude*) degree (Hons.) in physics from Brown University, Providence, RI, USA, in 1974; the M.S. and Ph.D. degrees in physics from the University of Illinois at Urbana-Champaign, Urbana, IL, USA, in 1975 and 1980, respectively; and an Honorary Doctorate degree, *Doctor Technish Honoris Causa*, from the Technical University of Denmark (DTU), Kongens Lyngby, Denmark in 2012.

Prof. Ziolkowski was the recipient of the 2019 IEEE Electromagnetics Award (IEEE Field Award). He is a Fellow of the Optical Society of America (OSA, 2006) and the American Physical Society (APS, 2016). He served as the President of the IEEE Antennas and Propagation Society in 2005. He is also actively involved with the URSI, OSA and SPIE professional societies. He was the Australian DSTO Fulbright Distinguished Chair in Advanced Science and Technology from 2014-2015. He was a 2014 Thomas-Reuters Highly Cited Researcher.

He is a Distinguished Professor in the Global Big Data Technologies Centre in the Faculty of Engineering and Information Technologies (FEIT) at the University of Technology Sydney, Ultimo NSW, Australia. He became a Professor Emeritus at the University of Arizona in 2018, where he was a Litton Industries John M. Leonis Distinguished Professor in the Department of Electrical and Computer Engineering in the College of Engineering and also a Professor in the College of Optical Sciences. He was the Computational Electronics and Electromagnetics Thrust Area Leader with the Engineering Research Division of the Lawrence Livermore National Laboratory, Livermore, CA, USA, before joining The University of Arizona, Tucson, AZ, USA, in 1990. His current research interests include the application of new mathematical and numerical methods to linear and nonlinear problems dealing with the interaction of electromagnetic and acoustic waves with complex linear and nonlinear media, as well as metamaterials, metamaterial-inspired structures, nano-structures, and other classical and quantum applications-specific configurations.